Molten salts etching strategy construct alloy/MXene heterostructures for efficient ammonia synthesis and energy supply via Zn-nitrite battery

Zhijie Cui [a],[1], Pengwei Zhao [b],[1], Honghai Wang [a], Chunli Li [a],[*], Wenchao Peng [b], Xiaobin Fan [b],[*], Jiapeng Liu [a],[*]

[a] School of Chemical Engineering and Technology, National-Local Joint Engineering Laboratory for Energy Conservation in Chemical Process Integration and Resources Utilization, Hebei University of Technology, Tianjin 300130, China
[b] School of Chemical Engineering and Technology, Tianjin University, Tianjin 300072, China

A B S T R A C T

The electrochemical nitrite reduction reaction (NO_2RR) is an environmentally friendly ammonia (NH_3) synthesis method. However, limited NH_3 yield and unsatisfactory faradaic efficiency seriously hindered the development of NO_2RR. Herein, the CuNi/MXene heterostructures were obtained using a bimetallic hybrid molten salt etching strategy, in which the Al layer of the MAX phase was successfully etched and the copper salt and nickel salt were simultaneously reduced to CuNi alloy nanoparticles (CuNi NPs) loaded on MXene. MXene as a support can effectively prevent CuNi NPs from agglomerating due to the metal-support interaction (MSI), thus exposing more active sites. Moreover, the alloying of copper and nickel causes the d-band center of copper to move towards the Fermi level, which enhances the adsorption of NO_2^- intermediates. As a result, the Cu_3Ni/MXene exhibited excellent NH_3 yield (10.22 mg h^{-1} mg$_{cat.}^{-1}$) and faradaic efficiency (95.6%). The Zn-NO_2^- battery with Cu_3Ni/ MXene demonstrated outstanding power density (8.34 mW cm^{-2}), NH_3 yield (1.91 mg h^{-1} mg$_{cat.}^{-1}$), and faradaic efficiency (90.3%), simultaneously achieving consumption of the pollutant nitrite, NH_3 synthesis and energy supply. Furthermore, the combination of in situ FTIR and DFT calculation aimed to elucidate the pathway and mechanism of NO_2RR, which will help to design high-performance catalysts.

1. Introduction

As an extremely valuable compound, ammonia (NH_3) is widely used in the chemical, agricultural and pharmaceutical industries [1–5]. At present, NH_3 is mainly produced by the Haber-Bosch process, which uses hydrogen and nitrogen as raw materials at a temperature of 400–600 °C and a high pressure of 20–50 MPa [6,7]. Extreme industrial conditions make the Haber-Bosch process responsible for approximately 2% of global CO_2 emissions, which means that the huge energy consumption seriously hinders the sustainable development of NH_3 synthesis [8–10]. In order to mitigate global energy consumption and achieve the goal of carbon neutrality, it is essential to find an environmentally friendly method for NH_3 production. As one of the recently developed methods, electrocatalytic reduction of nitrogen-containing species to ammonia (ERNA) has received wide attention because of its simple operation, high safety and low energy consumption [11,12]. ERNA uses water and nitrogenous compounds (nitrogen, nitric oxide, nitrate, and nitrite) as

feedstock, avoiding the large CO_2 emissions that result from the hydrogen production process in conventional NH_3 synthesis [13–18]. Compared with other nitrogen-containing compounds, nitrite (NO_2^-) has very high solubility in water and low bond breaking energy, which makes the electrochemical nitrite reduction reaction (NO_2RR) show great application potential in the field of green NH_3 synthesis [19–21]. Moreover, the high reduction potential (0.897 V vs. RHE at pH=0) of NO_2^- facilitates the generation of electrical energy, thus providing a higher current and power density. Therefore, replacing the oxygen evolution reaction (OER) with zinc dissolution/deposition at the anode and coupling with NO_2RR at the cathode can be assembled into an electrocatalytic system with dual functions (NH_3 synthesis and energy supply) [6,22–24]. The Zn-NO_2^- battery is considered to be a three birds with one stone strategy for pollutant consumption of nitrite, NH_3 synthesis and energy supply [25].

It is widely known that the NH_3 yield and faradaic efficiency are highly dependent on the performance of the catalysts [26].

---

* Corresponding authors.
E-mail addresses: lichunli_hebut@126.com (C. Li), xiaobinfan@tju.edu.cn (X. Fan), liujiapeng@hebut.edu.cn (J. Liu).
[1] These authors contributed equally to this work.

Copper-based catalysts, which are characterized by low cost and high activity, are one of the most promising electrocatalysts for NH_3 synthesis by nitrite reduction [27–31]. However, the limited catalytic active sites of copper-based catalysts result in low NH_3 yields and faradaic efficiencies [32]. Alloying copper with other metals (Ni, Co, Fe, Pt, Pd, Ru and Au) is an effective strategy to enhance the performance of NO_2RR [32–38]. In addition, supports are usually used to improve the dispersion of pure phase alloy nanoparticles, which can expose more active sites and improve stability [39,40]. As a rising star in the family of two-dimensional materials, transition metal carbon (nitrogen) compound (MXene) is an ideal support for metal loading due to its unique electronic structure, satisfactory electrical conductivity and excellent mechanical strength [41,42]. The metal-support interaction (MSI) can make the metal nanoparticles uniformly load on MXene, which is conducive to improving the stability of the catalyst [43,44]. However, on the one hand, the composite methods of MXene and metal are often complicated. The whole process firstly requires the synthesis of multiple or fewer layers of MXene by etching the MAX phase, followed by electrostatic adsorption of MXene with metal ion solutions, and finally a complex post-treatment. On the other hand, MXene is usually prepared by etching the Al layer of the MAX phase with fluorine-containing reagents (HF, NH_4F, LiF + HCl mixture) as an etchant. The highly hazardous fluorinated reagents can lead to significant safety hazards and environmental pollution. As a green etching method, Lewis acidic molten salt etching can avoid the use of fluorinated reagents [45]. Notably, metal ions are reduced to metal particles supported on MXene during molten salt etching process, but it is usually post-processed to obtain pure-phase MXene. Based on the above considerations, without post-treatment after the molten salt etching, not only the residual metal can be used as the active site of NO_2RR, but also the recombination step of metal and MXene can be effectively simplified. Furthermore, the MAX phase was etched by different molten salts ($CuCl_2$ and $NiCl_2·6H_2O$). Cu^{2+} and Ni^{2+} can be co-reduced to CuNi alloy nanoparticles (CuNi NPs) and in-situ loaded on MXene support. To our knowledge, the co-reduction of two metal ions into alloy by bimetallic mixed molten salts and in situ loading on MXene have not been reported, which makes it extremely valuable to explore the application in NO_2RR and Zn-NO_2^- batteries.

Herein, the CuNi/MXene heterostructures were obtained using a bimetallic mixed molten salt etching strategy, in which the Al layer of the MAX phase was successfully etched and the copper salt and nickel salt were simultaneously reduced to CuNi alloy nanoparticles (CuNi NPs) loaded on MXene. On the one hand, MXene as a support can effectively prevent CuNi NPs from agglomerating due to the metal-support interaction (MSI), thus exposing more active sites. On the other hand, the alloying of copper and nickel causes the d-band center of copper to move towards the Fermi level, which enhances the adsorption of NO_2^- intermediates. Benefiting from the enhanced intermediate adsorption and the interaction between CuNi NPs and MXene, Cu_3Ni/MXene exhibited excellent NH_3 yield (10.22 mg h^{-1} $mg_{cat.}^{-1}$) and Faradaic efficiency (95.6%) at −0.6 vs. RHE (reversible hydrogen electrode). Based on the excellent NO_2RR performance of Cu_3Ni/MXene, a Zn-NO_2^- battery was assembled with Cu_3Ni/MXene as the cathode catalyst. The battery demonstrated impressive power density (8.34 mW cm^{-2}), NH_3 yield (1.91 mg h^{-1} $mg_{cat.}^{-1}$ at 10 mA cm^{-2}), and Faradaic efficiency (90.3%), which successfully achieving simultaneous consumption of the pollutant nitrite, NH_3 synthesis and energy supply. More importantly, electrochemical in situ Fourier transform infrared spectroscopy (FTIR) and density functional theory (DFT) calculations were combined to elucidate the pathway and mechanism of NO_2RR, thereby contributing to the design and optimization of high-performance catalysts.

2. Experimental section

2.1. Preparation of samples

The synthesis of Cu_3Ni/MXene is taken as an example, 0.5 g Ti_3AlC_2, 0.78 g $CuCl_2$ and 0.46 g $NiCl_2·6H_2O$ were mixed and ground in Ar atmosphere for 10 min. Then 0.3 g NaCl and 0.38 g KCl were added to the mixture and ground for another 10 min in Ar atmosphere. The mixture was placed in an alumina boat and put in a tubular furnace. The mixture was heated to 750 °C at the rate of 4 °C/min in Ar atmosphere for 24 h and then cooled down naturally. The powder was thoroughly cleaned with deionized water, refrigerated and freeze-dried to obtain the final product. The molar ratio of Ti_3AlC_2: metal salt: NaCl: KCl remains 1:3:2:2. The preparation process of other samples is similar to the above steps, except that the mass of reactants used is different (Table 1). In order to better compare the properties between the samples, pure MXene was prepared. 0.1 g Ni/MXene was added to 100 mL of 2 M HCl and stirred for 36 h to completely remove Ni NPs. The resulting solution was washed with deionized water. Finally, the MXene powders were obtained by freeze-drying for 24 h.

2.2. Characterization

The crystal structure of the products was verified by X-ray diffraction (XRD, Bruker, Cu Kα radiation). Scanning electron microscopy (SEM, Tescan MIRA LMS) and transmission electron microscopy (TEM, Tescan MIRA LMS) were used to examine the morphology and elemental distribution of the products. The surface chemistry information of the products was analyzed by X-ray photoelectron spectroscopy (XPS, Thermo Scientific K-Alpha). Electrochemical in situ Fourier transform infrared (FTIR) spectroscopy was performed on the Bruker VERTEX 70 V spectrometer to detect reaction intermediates. The N_2 adsorption/desorption isotherms were obtained by Micromeritics ASAP 2460. Transmission XAS measurements were performed on a laboratory device (easyXAFS300, easyXAFS LLC), which is based on Rowland circle geometries with spherically bent crystal analyzers (SBCA) and operated using an Ag X-ray tube source and a silicon drift detector (AXAS-M1, KETEK GmbH).

2.3. Electrochemical characterization methods

The linear sweep voltammetry (LSV), cyclic voltammetry (CV), chronoamperometry, and electrochemical impedance spectrum (EIS) tests were performed on the CHI-760E electrochemical workstation using a three-electrode system, in which the carbon paper supported catalysts (1 × 1 cm^2), Ag/AgCl (3 M KCl), and platinum wire were used as the working electrode, reference electrode and counter electrode, respectively. The NO_2RR test was measured in an Ar-saturated electrolyte of 0.5 M K_2SO_4 + 0.05 M KNO_2 using a H-type cell, which was separated by a Nafion 117 membrane. The Nafion 117 membrane was firstly treated with 5 wt% hydrogen peroxide (H_2O_2) at 80 °C for 1 h and then soaked in deionized water for 0.5 h. It is then boiled in 5 wt% sulfuric acid (H_2SO_4) for 1 h at 80 °C and finally in deionized water for 0.5 h at 80 °C. The preparation steps of the working electrode were as follows: 10 mg of catalysts were dispersed in a mixed solution (0.45 mL of deionized water + 0.45 mL of anhydrous ethanol + 50 μL of Nafion

Table 1
The detailed molar ration of each substance in the molten salt etching strategy.

Catalysis	Ti_3AlC_2	$CuCl_2$	$NiCl_2·6H_2O$	NaCl	KCl
Cu/MXene	1	3	/	2	2
Ni/MXene	1	/	3	2	2
Cu_3Ni/MXene	1	2.25	0.75	2	2
CuNi/MXene	1	1.5	1.5	2	2
$CuNi_3$/MXene	1	0.75	2.25	2	2

solution) and ultrasonic treatment was carried out for 1 h to form a uniform ink. 50 μL of catalyst ink droplets were applied to carbon paper (1×1 cm^2) and dried at room temperature. The supported mass of catalyst was determined to be 0.5 mg cm^{-2}. All potentials in this work refer to RHE, and the conversion can be calculated by the Eq. 1:

$$E(RHE) = E(Ag/AgCl) + 0.222 + 0.059 \times pH \quad (1)$$

Electrochemical active surface area (ECSA) can be calculated by the Eq. 2:

$$ECSA = \frac{Cdl \times S}{C_s} \quad (2)$$

Where Cdl is the double layer capacitance. C_s and S represent specific capacitance (0.04 mF cm^{-2}) and electrode area (1×1 cm^2), respectively.

2.4. DFT calculation details

All the density function theory (DFT) calculations were carried out using the Vienna Ab initio Simulation Package (VASP). The ionic cores were described with projector augmentedwave (PAW) pseudopotential and take valence electrons into account using a plane wave basis set with a kinetic energy cutoff of 500 eV. The Perdew-Burke-Ernzerhof (PBE) functional was employed to describe exchange-correlation effects of electrons. The dimension of a 4×4 supercell of Cu (111) and Cu$_3$Ni (111) with a sufficient vacuum layer of 20 Å thicknesses. For the geometrical optimizations, a $3 \times 3 \times 1$ Γ-centered Monkhorst-Pack schemed k-mesh was set to sample the first Brillouin zone. The DFT-D3 method included the long-range van der Waals interaction. The convergence criterion for the electronic self-consistent field (SCF) loop was set to 10^{-5} eV/atom. The atomic structures were optimized until the residual forces were below 0.02 eV Å^{-1}.

3. Results and discussion

3.1. Materials synthesis and characterization

The synthesis route of the Cu$_x$Ni$_y$/MXene heterostructure is shown in Fig. 1. In brief, the Cu$_x$Ni$_y$/MXene heterostructure was obtained by etching the MAX phase using a mixture of molten salts of CuCl$_2$ and NiCl$_2$·6H$_2$O and then removing the residual molten salts. During the etching process, Cu^{2+} and Ni^{2+} can oxidize Al to Al^{3+} to form the volatile AlCl$_3$ due to the weak bonding of exposed Al to Ti, while Cu^{2+} and Ni^{2+} are co-reduced to CuNi NPs. Meanwhile, MXene can be endowed with the surface functional groups of −O and −Cl by charge compensation [45].

The crystalline phase of the prepared catalyst was characterized by X-ray diffraction (XRD) (Fig. 2a). Compared to the MAX phase, the (002) and (004) peaks of Cu/MXene, Ni/MXene and Cu$_x$Ni$_y$/MXene are displaced from 9.55°/19.19° to 7.87°/15.93° and the layer spacing increases from 9.25 Å to 11.34 Å. This result indicates that the Al layer in the MAX phase is successfully etched, which is consistent with the pure MXene (Fig. S1)[46]. In addition, the XRD spectra of Cu/MXene and Ni/MXene have diffraction peaks at 43.4°, 50.5°, 74.2° and 44.4°, 51.7°, 76.3°, corresponding to the (111), (200), and (220) crystal planes of cubic Cu and Ni, respectively [33]. In the XRD pattern of Cu$_x$Ni$_y$/MXene, except for the diffraction peaks of CuNi, no single component Cu and Ni diffraction peaks are detected, indicating the alloying of Cu and Ni. Interestingly, it is observed that the angle of the CuNi diffraction peak decreases with increasing Cu loading (Fig. 2b). This phenomenon is due to the fact that the atomic radius of Cu is larger than that of Ni, extending the lattice spacing of CuNi NPs. The above results show that Cu^{2+} and Ni^{2+} are co-reduced to CuNi NPs during molten salt etching, which proves the successful alloying of Cu and Ni. The specific surface area (SSA) of the samples was analyzed by using nitrogen isothermal adsorption and desorption curves. As shown in Fig. S2, the SSA of MXene, Cu/MXene, Ni/MXene, and Cu$_3$Ni/MXene are 21.3, 43.2, 46.7, and 58.9 m^2 g^{-1}, respectively. Compared with pure MXene, the SSA of the heterostructures is significantly increased, which is attributed to the supporting role of metal NPs in the MXene interlayer [47]. The increased SSA not only exposes more catalytic active sites, but also promotes electrolyte penetration [48]. The surface chemical states and bonding information of Cu/MXene, Ni/MXene and Cu$_3$Ni/MXene were analyzed by X-ray photoelectron spectroscopy (XPS). In the full range of the XPS spectrum on Cu$_3$Ni/MXene (Fig. S3), the characteristic peaks of Cu 2p and Ni 2p also prove that CuNi NPs are successfully loaded on MXene, and similar results are obtained for Cu/MXene and Ni/MXene. In the high-resolution Ti 2p spectra (Fig. 2c), the peaks of all samples can be deconvoluted into Ti−C (I) (454.7/460.4 eV), Ti−C (II) (455.5/461.2 eV), Ti−Cl (456.6/462.8 eV) and Ti−O (458.1/464.0 eV). The presence of Ti−C (I) and Ti−C (II) indicates the successful preparation of MXene with Ti$_6$C octahedral structure [49]. In the high-resolution spectra of C 1 s (Fig. 2d) and O 1 s (Fig. 2e), the characteristic peaks of C−O (286.2 eV), C−Cl (288.6 eV) and Ti−O (529.6 eV) can also prove the presence of O and Cl groups on the surface of MXene [45]. More importantly, it can be observed that the Ti−O−M (M=Cu, Ni and Cu$_3$Ni) of the three samples in the high-resolution O 1 s spectrum indicates that the metal nanoparticles are bound to the MXene support with O as the connection point [47]. The appearance of Ti−O−M bond further proves the formation of heterostructure, and MSI within the heterostructure can guarantee rapid electron transfer between metal NPs and MXene [50,51]. The high-resolution Cu 2p spectra
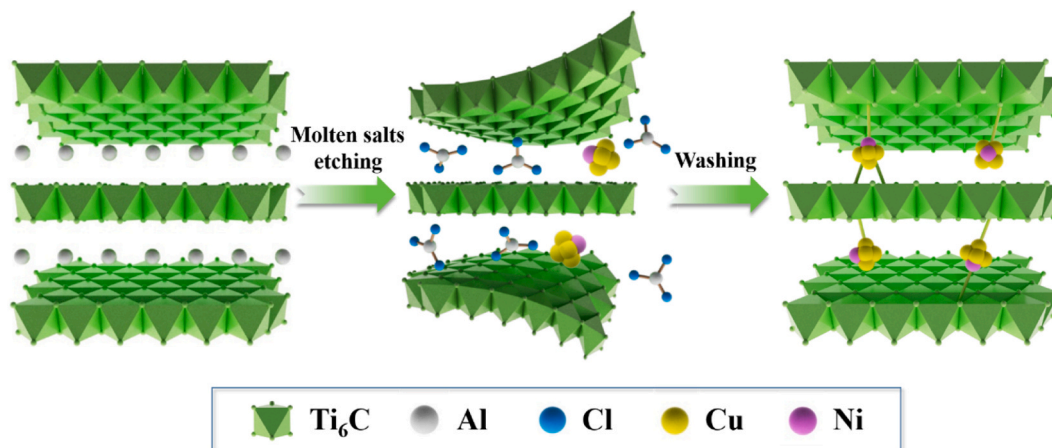

Fig. 1. The composite diagram of Cu$_x$Ni$_y$/MXene.

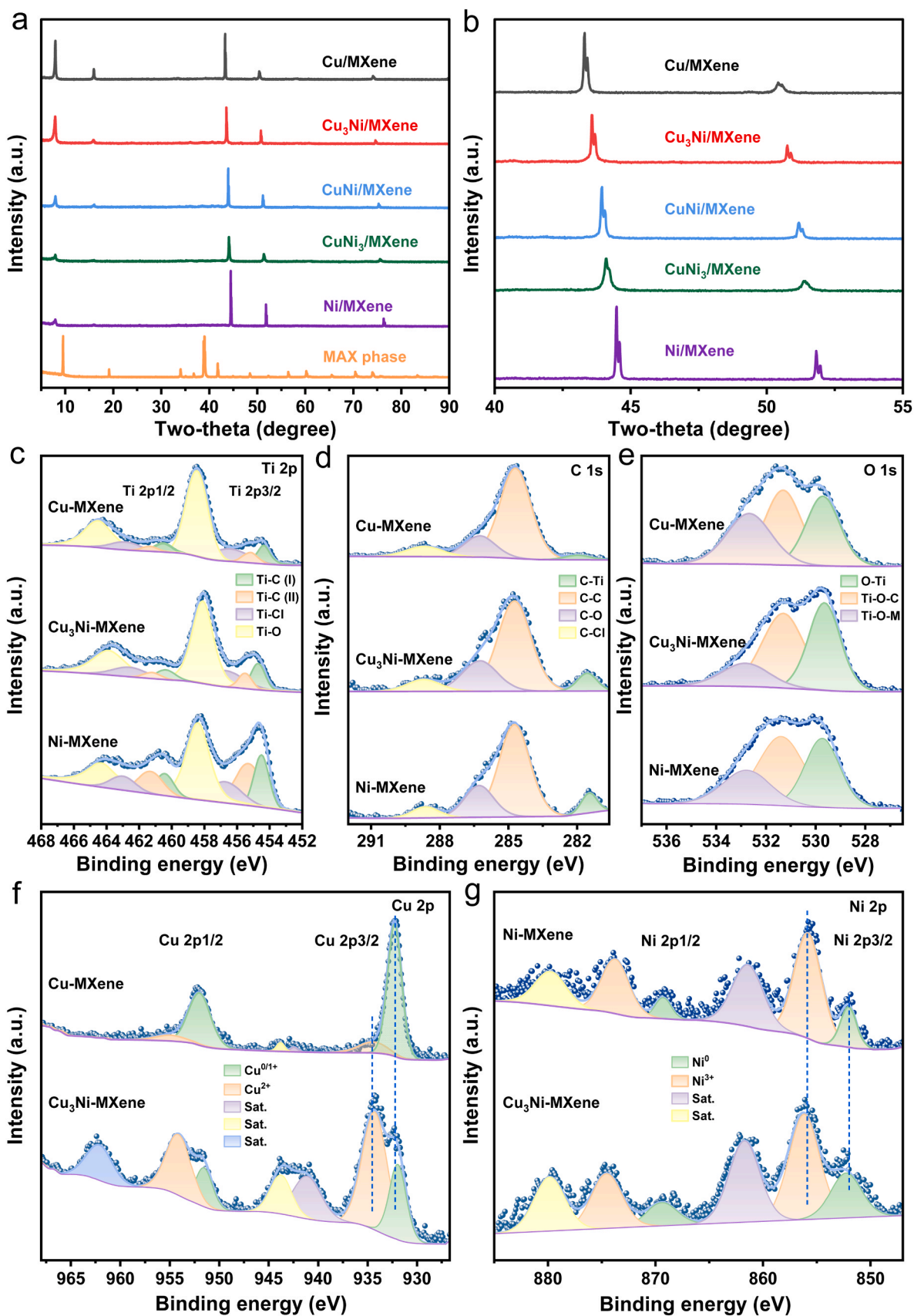**Fig. 2.** (a) XRD pattern and (b) Partial enlarged region of MAX phase, Cu/MXene, Ni/MXene and Cu$_x$Ni$_y$/MXene. High-resolution XPS spectrum of (c) Ti 2p, (d) C 1 s, (e) O 1 s, (f) Cu 2p and (g) Ni 2p.

of Cu/MXene and Cu₃Ni/MXene can be fitted to the Cu$^{0/1+}$ and Cu^{2+} characteristic peaks. Compared with Cu/MXene, the Cu 2p binding energy of Cu₃Ni/MXene undergoes a certain blueshift of 0.2 eV (Fig. 2f and Table S1). Interestingly, the opposite pattern was observed in the high-resolution Ni 2p spectra. Compared with Ni/MXene, the Ni 2p binding energy of Cu₃Ni/MXene has a redshift of 0.2 eV (Fig. 2g and Table S1). The above results show that electron rearrangement occurs between Cu and Ni, and Cu gets electrons provided by Ni [33].

In order to further study the electronic structure and atomic coordination environment of Cu₃Ni alloy NPs in Cu₃Ni/MXene, X-ray absorption near-edge structure (XANES) and extended X-ray absorption

fine structure (EXAFS) spectra were performed. The XANES spectra of Cu K-edge and Ni K-edge show that the near-edge absorption energy of Cu₃Ni/MXene is located near Cu foil and Ni foil, indicating the intrinsic valance state of Cu and Ni (Fig. 3a-b). The Cu K-edge and Ni K-edge energy of Cu₃Ni/MXene shows a slight shift compared to the metal reference, which demonstrates the electron transfer and strong Cu-Ni coupling. The Fourier-transformed EXAFS (FT-EXAFS) spectrum of Cu K-edge in Cu₃Ni/MXene has a strong peak at 2.2 Å, which is consistent with the Cu-Cu characteristic peak of Cu foil (Fig. 3c-d). Similarly, the strong peaks in the FT-EXAFS spectrum of Ni K-edge are consistent with the Ni-Ni characteristic peaks of Ni foil (Fig. 3e-f). Notably, the Cu-Cu/
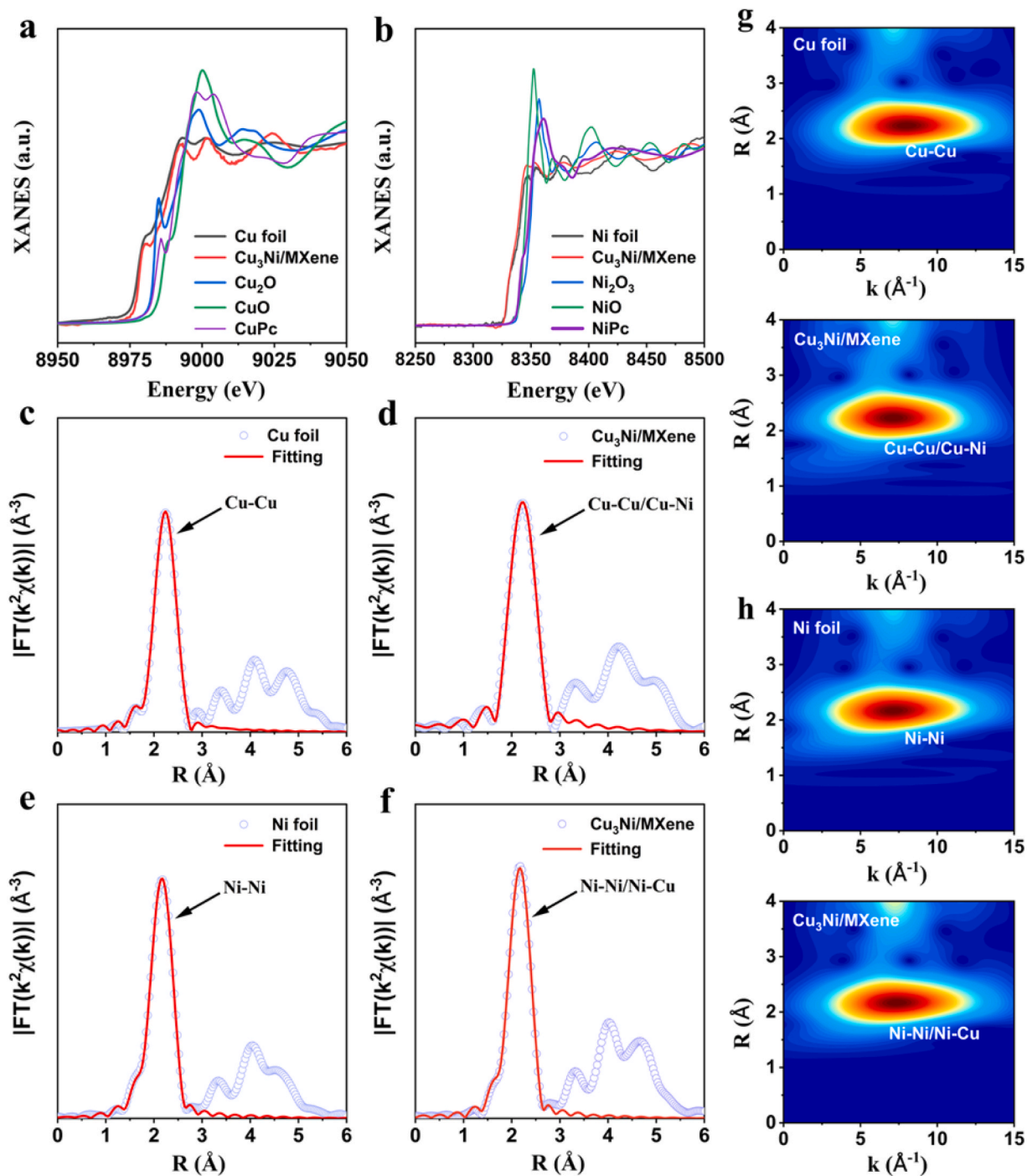

Fig. 3. (a) Cu K-edge XANES of Cu₃Ni/MXene, Cu foil, Cu₂O, CuO and CuPc. (b) Ni K-edge XANES of Cu₃Ni/MXene, Ni foil, Ni₂O₃, NiO and NiPc. The Cu K-edge EXAFS fitting curves of (c) Cu foil and (d) Cu₃Ni/MXene at R space. The Ni K-edge EXAFS fitting curves of (e) Ni foil and (f) Cu₃Ni/MXene at R space. (g) Wavelet transforms of Cu K-edge EXAFS signals of Cu foil and Cu₃Ni/MXene. (h) Wavelet transforms of Ni K-edge EXAFS signals of Ni foil and Cu₃Ni/MXene.

Cu-Ni characteristic peak in Cu$_3$Ni/MXene shows slightly smaller bond length compared to the Cu-Cu characteristic peaks in Cu foil, which is attributed to the synergistic effect of Cu and Ni in the structure. The Cu K-edge wavelet transform (WT-EXAFS) of Cu$_3$Ni/MXene shows a contour peak with a maximum intensity of about 7.5 Å^{-1}, which is close to that of Cu-Cu in Cu foil (Fig. 3g). The Ni K-edge WT-EXAFS of Cu$_3$Ni/MXene shows a contour peak similar to the Ni-Ni of Ni foil (Fig. 3h). These results proved the presence of Cu-Cu/Cu-Ni and Ni-Ni/Ni-Cu coordination in the structure of Cu$_3$Ni/MXene [33,52]. The bonding conditions and coordination environment of Cu and Ni were further determined by EXAFS fitting results (Fig. S4a-d). With Cu foil and Ni foil as reference, the Cu and Ni EXAFS fitting curves of Cu$_3$Ni/MXene are highly consistent with the structure of Cu$_3$Ni alloy in R and K space, which proves the Cu$_3$-Ni coordination structure. In addition, the EXAFS coordination information table of Cu$_3$Ni/MXene (Table S2) shows that the coordination ratio (CN) of Cu and Ni is about 3 (7.2:2.3), which supports the EXAFS fitting results.

The morphology and crystal structure of the catalysts were investigated by field-emission scanning electron microscopy (FESEM) and transmission electron microscopy (TEM). In the FESEM images of Cu$_3$Ni/MXene (Fig. 4a-b), it can be easily seen that the MAX phase was successfully etched into an accordion shape and a large number of CuNi NPs were uniformly distributed on the surface and between the layers of the multilayer MXene. As shown in the TEM image of Fig. 4c, CuNi NPs can be clearly observed on the layered structure of Cu$_3$Ni/MXene. The high-resolution TEM images (Fig. 4d) show that the lattice spacing of CuNi (111) is 0.209 nm, which is smaller than that of Cu (0.212 nm) [33,49,52]. Since the atomic radius of Ni is smaller than that of Cu, the

alloying of Cu and Ni compresses the lattice of Cu, resulting in a stronger interaction force between Cu and Ni [53]. Notably, the lattice fringe (d = 1.13 nm) is attributed to the (002) crystal plane of MXene, indicating that MXene and CuNi NPs formed a heterostructure [47]. In addition, the diffraction rings of the (111), (200), and (220) crystal planes of CuNi NPs and the (002) crystal plane of MXene can also be observed in the selected area electron diffraction (SAED) of Cu$_3$Ni/MXene (Fig. 4e), which further confirms the formation of the heterostructure of MXene and CuNi NPs. The formation of heterostructure between CuNi NPs and MXene is conducive to enhancing the interaction between metal and support, which can improve the NO$_2$RR performance of CuNi/MXene. The HAADF-STEM images and corresponding energy dispersive spectrometer (EDS) show a homogeneous distribution of C, Ti, Cu, Ni, Cl, and O elements on the MXene support (Fig. 4f). The uniform dispersion of the CuNi NPs on MXene further demonstrates the role of MSI [54].

3.2. Electrocatalytic nitrite reduction performances of catalysts

In order to explore the electrochemical properties and NO$_2$RR performance of the synthesized catalysts, a typical three-electrode system was assembled for testing. The linear sweep voltammetry (LSV) curves of the five samples are shown in Fig. 5a. Compared to the electrolyte without the addition of NO$_2^-$, the current density of samples was significantly increased when NO$_2^-$ was added, indicating the occurrence of nitrite reduction. Among the different molar ratios of CuNi/MXene catalysts, Cu$_3$Ni/MXene exhibited the largest LSV reduction currents over the measured voltage range (from −1.1 V to 0.2 V vs. RHE). More excitingly, Cu$_3$Ni/MXene showed the smallest overpotential, indicating

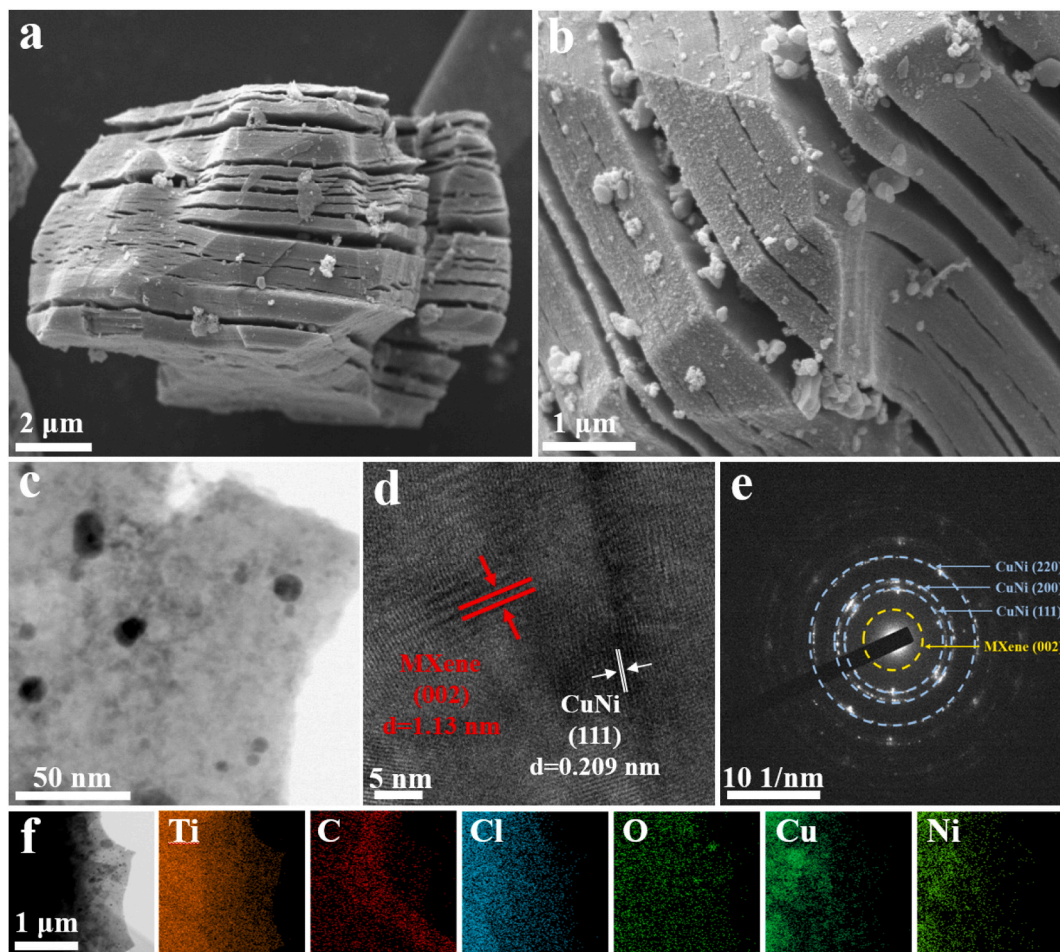**Fig. 4.** (a-b) FESEM images of Cu$_3$Ni/MXene. (c) TEM and (d) HRTEM images of Cu$_3$Ni/MXene. (e) SAED image of Cu$_3$Ni/MXene. (f) HAADF-STEM and EDS mapping images of Cu$_3$Ni/MXene.
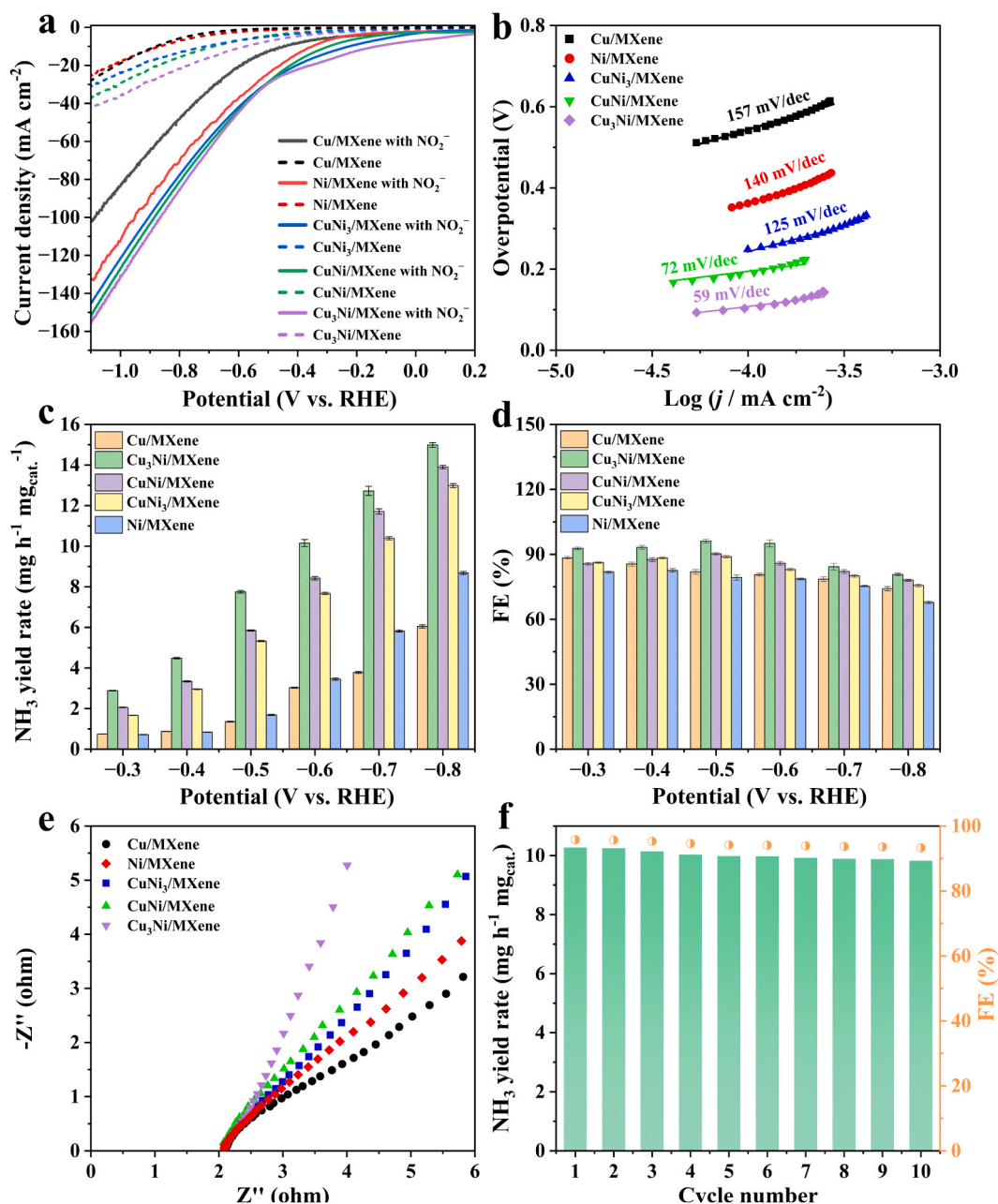
Fig. 5. (a) LSV curves with/without 0.05 M NO_2^- and (b) corresponding Tafel slope of Cu/MXene, Ni/MXene and Cu_xNi_y/MXene. (c) NH_3 yield and (d) corresponding Faradaic efficiency of Cu/MXene, Ni/MXene and Cu_xNi_y/MXene at different potentials. (e) EIS measurement of Cu/MXene, Ni/MXene and Cu_xNi_y/MXene. (f) NH_3 yield and Faradaic efficiency of Cu_3Ni/MXene for 10 cycles at −0.6 V vs. RHE.

that Cu_3Ni/MXene possesses low energy consumption and outstanding electrocatalytic activity in the NO_2RR process [6,55]. In addition, the corresponding Tafel slope can be obtained according to the LSV curves of each sample (Fig. 5b). The Tafel slope of Cu_3Ni/MXene is only 59 mV/dec, which indicates that Cu_3Ni/MXene has a faster reduction kinetics of nitrite [16,19,39].

In order to investigate the NO_2RR performance of the catalysts, all samples were tested by chronoamperometry measurement (Fig. S5a-e) and the concentration of NH_3 (Fig. S6a-b), NO_2^- (Fig. S7a-b) and N_2H_4 (Fig. S8a-b) generated in the electrolyte was detected by the ultraviolet and visible spectrophotometry (UV-Vis). As shown in Fig. 5c, the NH_3 yield of Cu_3Ni/MXene was significantly higher than other samples at all operating voltages, which is consistent with the LSV results. More importantly, the NH_3 yield of different molar ratios of CuNi/MXene was all much greater than Cu/MXene and Ni/MXene, which is further

evidence that the NO_2RR performance of the bimetallic catalysts (Cu_xNi_y/MXene) is superior to the monometallic catalysts (Cu/MXene and Ni/MXene). It is worth noting that Cu_3Ni/MXene has an excellent Faradaic efficiency over a wide voltage range, which indicates that Cu_3Ni/MXene can effectively inhibit the occurrence of side reactions (Fig. 5d). Notably, Cu/MXene exhibits a higher Faradaic efficiency than Ni/MXene, while Ni/MXene exhibits a greater NH_3 yield than Cu/MXene. As the active sites of NO_2RR, Cu and Ni have different catalytic roles, in which Cu is responsible for the adsorption and deoxidation of NO_2^-, and Ni is responsible for providing protons for the subsequent hydrogenation reaction. For monometallic catalysts, due to the lack of sufficient proton supply, a large amount of NO_2^- accumulated on Cu/MXene cannot be converted into NH_3 in time, thus reducing the NH_3 production rate [6,20]. Due to the rapid hydrogen evolution kinetics and the relatively sluggish NO_2RR kinetics of Ni, the hydrogen evolution

reaction (HER) will be aggravated, resulting in a lower Faradaic efficiency of Ni/MXene. Therefore, the alloying of Cu and Ni can balance the deoxidation and hydrogenation processes of NO_2RR, which is conducive to greatly improving the NO_2^- reducing activity of CuNi/MXene. In addition, the proportion of CuNi alloying has an important effect on the performance of NO_2RR. At relatively low potentials (−0.3 and −0.4 V vs. RHE), the Faradaic efficiency of $CuNi_3$/MXene is higher than that of CuNi/MXene due to the weak degree of HER and the dominance of NO_2RR [26,56]. With the increase of potential (from −0.5 to −0.8 V vs. RHE), the Faradaic efficiency of $CuNi_3$/MXene with more Ni is less than CuNi/MXene due to the intensification of the HER. The above results indicate that the hydrogen evolution rate of Ni/MXene is faster than the NO_2^- reduction rate of Cu/MXene. Therefore, an appropriate increase of Cu in CuNi alloy is beneficial to the dynamic balance between HER and NO_2RR [57]. When the ratio of Cu and Ni is 3:1, the optimized catalyst (Cu_3Ni/MXene) possessed an excellent NH_3 yield of 10.22 mg h^{-1} mg$_{cat.}^{-1}$ and a satisfactory Faradaic efficiency of 95.6% at −0.6 V vs. RHE, which was 3.4 times (3.02 mg h^{-1} mg$_{cat.}^{-1}$) and 1.2 times (80.4%) higher than that of Cu/MXene, respectively. Cu_3Ni/MXene showed superior NO_2RR performance compared to most of reported materials (Table S3) [21,37,58–64]. In addition, the NO_2RR performance of pure MXene was further investigated. After electrolysis at different potentials, the maximum NH_3 yield and Faradaic efficiency of MXene (Fig. S9a-b) are only 1.16 mg h^{-1} mg$_{cat.}^{-1}$ and 41.3%, which is much smaller than those as-prepared samples containing metal/alloy NPs. These results further prove that the main catalytic active site is metal/alloy NPs. The NH_3 yield was verified by the ^1H Nuclear Magnetic Resonance (NMR) method (Fig. S10a-b), and the result was almost consistent with that of the indophenol blue method (Fig. S11). More importantly, the nitrogen balance was better understood by the detection of other products in the NO_2RR process. As shown in Fig. S12a-j, the main products of the five samples are NH_3 and H_2, as well as a very small amount of hydrazine (N_2H_4) and other nitrogen-containing gases (N_2 and NO, etc.), which indicates that most of the NO_2^- is generated into NH_3 through a series of deoxidation and hydrogenation steps. In order to eliminate the interference of external factors on NH_3 detection, a series of blank controlled experiments were conducted (Fig. S13). In the electrolyte without nitrite, no NH_3 was detected at either the operating voltage or the open-circuit voltage. As shown in Fig. S14a-j, Cu_3Ni/MXene exhibits the largest Cdl (2.37 mF cm^{-2}), which demonstrates that Cu_3Ni/MXene has more active sites to participate in the NO_2RR [65]. The electrochemical impedance spectroscopy (EIS) analysis in Fig. 5e shows that Cu_3Ni/MXene has a larger slope in the low frequency region, indicating that the alloying of Cu and Ni promotes the diffusion kinetics of ions at the contact interface between catalyst and electrolyte [66,67]. The electrochemical stability of Cu_3Ni/MXene for NO_2RR was investigated in Fig. 5f. After 10 consecutive electrolysis at −0.6 vs. RHE, the NH_3 yield (9.82 mg h^{-1} mg$_{cat.}^{-1}$) and Faradaic efficiency (93.3%) of Cu_3Ni/MXene decayed by only 5% and 3%, showing the superior stability of Cu_3Ni/MXene.

In general, nitrite shows a wide concentration range due to different sources of water quality (domestic water and industrial wastewater). Therefore, the catalytic performance of Cu_3Ni/MXene at different NO_2^- concentrations was studied to demonstrate its wide adaptability. In addition to the 0.05 M NO_2^- concentration, 0.025 M and 0.075 M NO_2^- concentrations were also selected to cover the concentration range in domestic and heavy industry wastewater [68]. As shown in Fig. S15a, the NH_3 yield increases with the increase of NO_2^- concentration and exhibits a maximum 17.2 mg h^{-1} mg$_{cat.}^{-1}$ at a NO_2^- concentration of 0.075 M and a voltage of −0.8 V. At different NO_2^- concentrations, Cu_3Ni/MXene exhibited a Faradaic efficiency of 90.5%, 95.6% and 92.3% at −0.6 V, respectively (Fig. S15b). These results suggest that Cu_3Ni/MXene exhibited high NH_3 yield and Faradaic efficiency over a wide NO_2^- concentration range. It is worth noting that when the nitrite concentration was 0.025 M, the NH_3 yield and Faradaic efficiency are relatively low due to the slow reaction kinetics of NO_2^-. When the

concentration of nitrite was 0.075 M, the active site on the catalyst surface was mostly covered by NO_2^- due to strong adsorption, which hindered the activation of *H and reduced the Faradaic efficiency of NO_2RR. Therefore, the appropriate concentration of NO_2^- can further improve the performance of NO_2RR by balancing the relationship between NO_2^- and *H. Due to the slow reaction kinetics, it is challenging to provide both high removal efficiency and high selectivity at low concentrations of NO_2^-. In order to evaluate the NO_2^- removal capacity of Cu_3Ni/MXene, electrolytic tests were performed with an electrolyte containing 300 ppm NO_2^-. As shown in Fig. S16a-b, Cu_3Ni/MXene exhibits NO_2^- conversion of 98.5% and NH_3 selectivity of 96.3%, indicating that almost all NO_2^- is removed and converted to NH_3 within 150 min. Notably, the concentration of NO_2^- decreased significantly to below the World Health Organization (WHO) drinking water standard (< 10 ppm) after 150 min of electrolysis. These results suggest that Cu_3Ni/MXene is a promising catalyst for the removal/conversion of NO_2^- in wastewater.

According to the above characterizations and experimental results, the excellent NO_2RR performance of Cu_3Ni/MXene heterostructure is attributed to the following points: (i) MXene as a support can provide high electrical conductivity, which is conducive to electron transfer during electrocatalytic reactions. In addition, the interlayer structure of MXene is able to provide more transport channels, which facilitates electrolyte permeation and ion diffusion. (ii) As the catalytic active site, the alloying of Cu and Ni optimizes the adsorption of NO_2^- and reduces the energy barrier of NO_2RR, which improves the yield and Faradaic efficiency of NH_3 synthesis. (iii) The metal-support interaction of the heterostructure can effectively prevent the agglomeration of CuNi alloy NPs during electrocatalysis. On the other hand, CuNi alloy NPs can also act as support frames for interlayer structures to prevent the structural collapse of MXene.

3.3. The performance of Zn-NO_2^- battery based on Cu_3Ni/MXene

Based on the excellent NO_2RR performance of Cu_3Ni/MXene, the aqueous Zn-NO_2^- battery device using the H-type cell was assembled. The open circuit voltage (OCV) of the aqueous Zn-NO_2^- battery was measured at 1.56 V and remained stable for 24 hours, indicating the superior potential of the battery (Fig. 6a). As can be seen from the discharge curve and power density curve of the battery in Fig. 6b, the peak power density of the battery reaches 8.34 mW cm^{-2}, which is much higher than those of most reported Zn-NO_2^-, Zn-NO_3^- and Zn-N_2 batteries (Table S4). The galvanostatic charge/discharge (GCD) process of the Zn-NO_2^- battery at a constant current density of 5 mA cm^{-2} (Fig. 6c). It can be observed that the voltage window remains almost the same width after 24 h of galvanostatic charge and discharge, indicating that the Zn-NO_2^- battery exhibits outstanding long-term electrochemical stability [25]. Excitingly, the assembled Zn-NO_2^- battery successfully powered the timer for 99 minutes (Fig. 6d), which is attributed to the excellent open circuit voltage, power density, and electrochemical stability. To investigate the NO_2RR performance of the Zn-NO_2^- battery, the NH_3 yield and Faradaic efficiency were tested at different current densities (Fig. 6e-f). At a current density of 10 mA cm^{-2}, the Zn-NO_2^- battery showed superior NH_3 yield (1.91 mg h^{-1} mg$_{cat.}^{-1}$) and excellent Faradaic efficiency (90.3%). The above results indicate that the Zn-NO_2^- battery with Cu_3Ni/MXene can simultaneously achieve the removal of nitrite pollutants, sustainable NH_3 synthesis and energy supply. In order to evaluate the practical application prospect of Zn-NO_2^- battery system, the techno-economic assessment is analyzed in detail [69]. As shown in Fig. S17, the revenue from the production of NH_3 and external energy supply of Zn-NO_2^- battery is expected to be roughly equal to the cost. Considering the potential environmental benefits of electrocatalytic NH_3 synthesis, the Zn-NO_2^- battery is undoubtedly a more competitive and attractive alternative strategy.
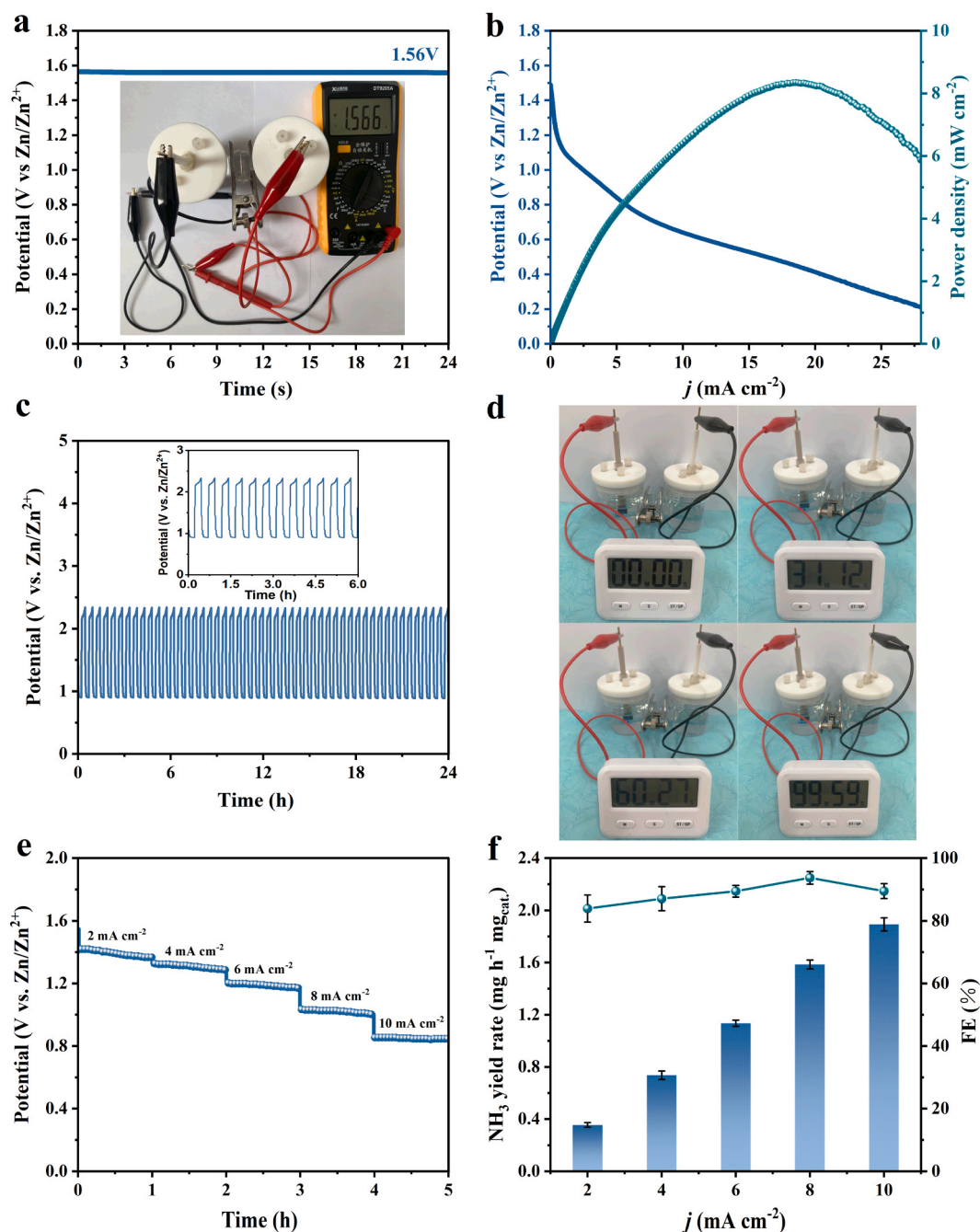
Fig. 6. (a) The OCP of the Cu₃Ni/MXene-based aqueous Zn-NO_2^- battery. (b) Discharge polarization curve and power density curve of the Zn-NO_2^- battery. (c) GCD curve of the Zn-NO_2^- battery. (d) Optical photo of the Zn-NO_2^- battery powered timer for 99 min. (e) Discharge curves and (f) corresponding NH₃ yield and Faradaic efficiency at different current densities.

3.4. The research of NO₂RR mechanism

The combination of electrochemical in situ Fourier transform infrared spectroscopy (FTIR) and density functional theory (DFT) calculations further illuminates the pathway and mechanism of NO₂RR. In situ FTIR was used to detect the intermediates of Cu/MXene and Cu₃Ni-MXene in the NO_2^- electrochemical reduction process. Specifically, in situ FTIR spectra of the catalysts in a 0.5 M K₂SO₄ electrolyte containing 0.05 M NO_2^-, where the infrared signals were collected from 1100 to 1600 cm^{-1}. In the resulting spectrum, the downward characteristic peak indicates the consumption of NO_2^-, and the upward characteristic peak indicates the formation of reaction intermediates (Fig. 7a-b). At open circuit voltage (OCP), no NO_2^- consumption or intermediates formation

can be observed, indicating that NO₂RR has not occurred on the catalyst surface. With the increase of the negative applied voltage, the vibration of the intermediate characteristic peak goes from weak to strong, which indicates that the NO₂RR is gradually activated. The upward characteristic peak at 1270 cm^{-1} attributed to the symmetric vibration mode of NO_2^-, which represents the consumption of NO_2^- [25]. The presence of characteristic peaks of NO intermediates at 1570 cm^{-1} and some NH$_x$ intermediates (−NH at 1175 cm^{-1} and H−N−H at 1420 cm^{-1}) confirms that deoxidation and hydrogenation steps occur during the NO_2^- reduction process [4]. More importantly, the peak at 1450 cm^{-1} is attributed to NH₄⁺, demonstrating the successful synthesis of NH₃ [4,67, 70]. Compared with Cu/MXene, the characteristic peak intensity of NO_2^- of Cu₃Ni/MXene is significantly increased, which indicates that the
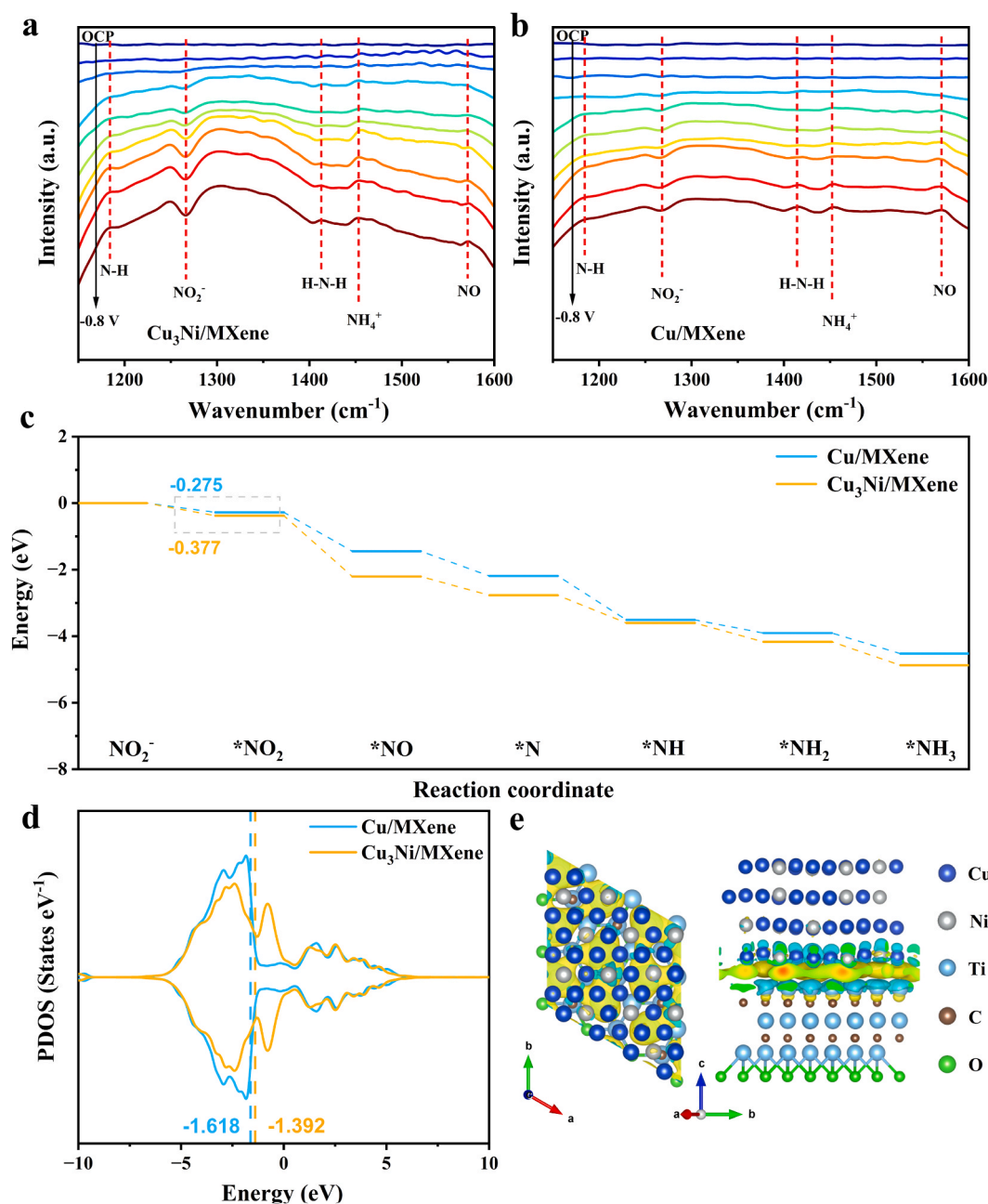
Fig. 7. (a) Electrochemical in situ FTIR spectroscopy of $Cu_3Ni/MXene$ and (b) Cu/MXene. (c) Gibbs free energy diagrams of Cu/MXene and $Cu_3Ni/MXene$ during the NO_2RR process. (d) PDOS of Cu/MXene and $Cu_3Ni/MXene$. (e) Differential charge density diagram of $Cu_3Ni/MXene$.

alloying strategy can enhance the adsorption of NO_2^-.

In order to explore mechanisms and the intrinsic properties of $Cu_3Ni/$ MXene activity enhancement of NO_2RR, detailed DFT calculations were performed. The reaction pathways of NO_2RR on Cu/MXene and $Cu_3Ni/$ MXene were established based on the intermediates observed by in-situ FTIR. According to the Gibbs free energy of each reaction step of NO_2RR (Fig. 7c), the reaction energy barrier of $* + NO_2^- \rightarrow *NO_2$ step on Cu/ MXene and $Cu_3Ni/MXene$ is -0.275 eV and -0.377 eV respectively, which is greater than the reaction energy barrier of the other steps. Therefore, $* + NO_2^- \rightarrow *NO_2$ is the most difficult reaction step to occur in this catalytic system, which proves that it is the rate-determining step (RDS). It is worth noting that $Cu_3Ni/MXene$ exhibited a lower energy barrier of RDS than Cu/MXene, proving that the alloying of Cu and Ni makes the NO_2RR process much easier to carry out. Surprisingly, $Cu_3Ni/$ MXene showed a lower energy barrier than Cu/MXene in the subsequent deoxidation hydrogenation steps, which indicates that $Cu_3Ni/MXene$

has excellent activity for NO_2^- reduction. In order to further investigate the ability of $Cu_3Ni/MXene$ to generate active hydrogen, the Gibbs free energy of HER process was calculated. HER consists of two steps ($^+H \rightarrow *H \rightarrow 1/2\ H_2$), where $^+H \rightarrow *H$ step promotes NO_2RR by providing $*H$ for the reduction of NO_2^-, and $*H \rightarrow 1/2\ H_2$ step is considered to be a competing reaction (HER) of NO_2RR. Therefore, the HER process is studied by constructing a series of $Cu_3Ni/MXene$ models with different hydrogen coverage. At less than 50% hydrogen coverage, $^+H \rightarrow *H$ step is a spontaneous exothermic process on the surface of $Cu_3Ni/MXene$, indicating its excellent ability to generate $*H$. In addition, the energy barriers of $*H \rightarrow 1/2\ H_2$ step on the surface of $Cu_3Ni/MXene$ at 0%, 25% and 50% hydrogen coverage are 0.42, 0.36 and 0.49 eV, which are much higher than the RDS energy barriers of NO_2RR (Fig. S18a). This result shows that $Cu_3Ni/MXene$ effectively inhibits the occurrence of HER and improves the selectivity of NO_2RR. It is worth noting that $H \rightarrow *H$ step exhibits an endothermic process with a high energy barrier (0.14 eV)

when the hydrogen coverage is 75%, which demonstrates that excessive hydrogen coverage will hinder the formation of *H (Fig. S18b). The above results indicate that moderate hydrogen coverage rate is more beneficial to hydrogenation process of NO_2RR. Therefore, $Cu_3Ni/MXene$ inhibits the occurrence of HER while promoting water splitting to *H, which improves the NH_3 yield and Faradaic efficiency of NO_2RR. The d-band center can accurately reflect the binding strength of the metal active center with the reactants and intermediates [33,71]. As shown in Fig. 7d, $Cu_3Ni/MXene$ (−1.392 eV) has a d-band center closer to the Fermi level than Cu/MXene (−1.618 eV), which indicates that the alloying of Cu and Ni enhances the adsorption energy in the intermediate. The strong adsorption of NO_2^- reduces the energy barrier of the RDS in the NO_2RR process, thus effectively improving the reducing activity of NO_2^-. Compared with Cu/MXene, the higher density state at the Fermi level means that $Cu_3Ni/MXene$ has higher conductivity, which is more conducive to electron conduction and charge transfer during the NO_2RR process [72]. In addition, the electrons of $Cu_3Ni/MXene$ are more arranged in bonding orbitals, which proves that the MSI between Cu_3Ni NPs and MXene reduces the overall system energy, resulting in higher structural stability [44]. To further understand the MSI, the charge density distribution on the surface of MXene loaded with Cu_3Ni NPs was calculated (Fig. 7e). It can be clearly observed that the electronic rearrangement occurs between Cu_3Ni NPs and MXene. Specifically, electrons are transferred from the Ti atom to the Cu_3Ni alloy atom present at the interface of the heterostructure, resulting in strong interfacial electron coupling between Cu_3Ni NPs and MXene.

4. Conclusions

In summary, the $Cu_xNi_y/MXene$ heterostructure was successfully synthesized by etching MAX phase with different molar ratios of bimetallic mixed molten salts ($CuCl_2$ and $NiCl_2\cdot6H_2O$). MXene as a support can effectively prevent CuNi NPs from agglomerating due to the MSI, thus exposing more active sites. Moreover, the alloying of copper and nickel causes the d-band center of copper to move towards the Fermi level, which enhances the adsorption of NO_2^- intermediates. Benefiting from the enhanced intermediate adsorption and the interaction between CuNi NPs and MXene, the optimized sample ($Cu_3Ni/MXene$) showed superior NO_2RR performance (NH_3 yield rate of 10.22 mg h^{-1} mg$_{cat.}^{-1}$ and Faradaic efficiency of 95.6%) at −0.6 vs. RHE. The Zn-NO_2^- battery with $Cu_3Ni/MXene$ not only exhibited a satisfactory power density of 8.34 mW cm^{-2} and successfully powered the timer, but also achieved a NH_3 yield of 1.91 mg h^{-1} mg$_{cat.}^{-1}$ and a Faradaic efficiency of 90.3% at a current density of 10 mA cm^{-2}. Furthermore, the combination of in situ FTIR and DFT calculation aimed to elucidate the pathway and mechanism of NO_2RR. Therefore, this work provides a simple and harmless method for the synthesis of bimetallic alloy catalysts based on MXene and a new way of thinking for combining energy-input electrocatalysis with energy-output batteries.

CRediT authorship contribution statement

Zhijie Cui: Investigation, Conceptualization, Methodology, Writing-original draft, Writing-review & editing. **Pengwei Zhao:** Data curation, Visualization, Software. **Honghai Wang:** Conceptualization. **Chunli Li:** Supervision, Writing - review & editing. **Wenchao Peng:** Data curation. **Xiaobin Fan:** Data curation, Writing-review & editing. **Jiapeng Liu:** Conceptualization, Supervision, Funding acquisition, Writing-original draft, Writing-review & editing.

Declaration of Competing Interest

The study of manuscript is original. No conflict of interest exits in the submission of this manuscript, and manuscript is approved by all authors for publication.

Data availability

Data will be made available on request.

Appendix A. Supporting information

Supplementary data associated with this article can be found in the online version at doi:10.1016/j.apcatb.2024.123862.

References

[1] J. Li, R. Chen, J. Wang, Y. Zhou, G. Yang, F. Dong, Subnanometric alkaline-earth oxide clusters for sustainable nitrate to ammonia photosynthesis, Nat. Commun. 13 (2022) 1098.

[2] Q. Song, M. Li, L. Wang, X. Ma, F. Liu, X. Liu, Mechanism and optimization of electrochemical system for simultaneous removal of nitrate and ammonia, J. Hazard. Mater. 363 (2019) 119–126.

[3] J. Theerthagiri, J. Park, H.T. Das, N. Rahamathulla, E.S.F. Cardoso, A.P. Murthy, G. Maia, D.V.N. Vo, M.Y. Choi, Electrocatalytic conversion of nitrate waste into ammonia: a review, Environ. Chem. Lett. 20 (2022) 2929–2949.

[4] G. Zhang, X. Li, K. Chen, Y. Guo, D. Ma, K. Chu, Tandem electrocatalytic nitrate reduction to ammonia on MBenes, Angew. Chem. Int. Ed. 62 (2023) e202300054.

[5] F. Jiao, B. Xu, Electrochemical ammonia synthesis and ammonia fuel cells, Adv. Mater. 31 (2019) 1805173.

[6] R. Zhang, Y. Guo, S. Zhang, D. Chen, Y. Zhao, Z. Huang, L. Ma, P. Li, Q. Yang, G. Liang, C. Zhi, Efficient ammonia electrosynthesis and energy conversion through a Zn-nitrate battery by iron doping engineered nickel phosphide catalyst, Adv. Energy Mater. 12 (2022) 2103872.

[7] S. Zhang, J. Wu, M. Zheng, X. Jin, Z. Shen, Z. Li, Y. Wang, Q. Wang, X. Wang, H. Wei, J. Zhang, P. Wang, S. Zhang, L. Yu, L. Dong, Q. Zhu, H. Zhang, J. Lu, Fe/Cu diatomic catalysts for electrochemical nitrate reduction to ammonia, Nat. Commun. 14 (2023) 3634.

[8] X. Li, X. Zhao, Y. Zhou, J. Hu, H. Zhang, X. Hu, G. Hu, Pd nanocrystals embedded in BC_2N for efficient electrochemical conversion of nitrate to ammonia, Appl. Surf. Sci. 584 (2022) 152556.

[9] B. Lee, L.R. Winter, H. Lee, D. Lim, H. Lim, M. Elimelech, Pathways to a green ammonia future, ACS Energy Lett. 7 (2022) 3032–3038.

[10] D. Zhu, B. Zhang, J. Chen, F. Xie, Y. Zou, P. Chen, CoFe nanoalloys encapsulated in nitrogen-doped carbon for efficient nitrite electroreduction to ammonia, Chem. Commun. 59 (2023) 9626–9629.

[11] A. Iarchuk, A. Dutta, P. Broekmann, Novel Ni foam catalysts for sustainable nitrate to ammonia electroreduction, J. Hazard. Mater. 439 (2022) 129504.

[12] J. Sun, S. Garg, J. Xie, C. Zhang, T.D. Waite, Electrochemical reduction of nitrate with simultaneous ammonia recovery using a flow cathode reactor, Environ. Sci. Technol. 56 (2022) 17298–17309.

[13] W.-J. Sun, L.-X. Li, H.-Y. Zhang, J.-H. He, J.-M. Lu, A. Bioinspired, Iron-centered electrocatalyst for selective catalytic reduction of nitrate to ammonia, ACS Sustain. Chem. Eng. 10 (2022) 5958–5965.

[14] Z.-Y. Wu, M. Karamad, X. Yong, Q. Huang, D.A. Cullen, P. Zhu, C. Xia, Q. Xiao, M. Shakouri, F.-Y. Chen, J.Y. Kim, Y. Xia, K. Heck, Y. Hu, M.S. Wong, Q. Li, I. Gates, S. Siahrostami, H. Wang, Electrochemical ammonia synthesis via nitrate reduction on Fe single atom catalyst, Nat. Commun. 12 (2021) 2870.

[15] J.M. McEnaney, S.J. Blair, A.C. Nielander, J.A. Schwalbe, D.M. Koshy, M. Cargnello, T.F. Jaramillo, Electrolyte engineering for efficient electrochemical nitrate reduction to ammonia on a titanium electrode, ACS Sustain. Chem. Eng. 8 (2020) 2672–2681.

[16] Y. Guo, X. Cai, S. Shen, G. Wang, J. Zhang, Computational prediction and experimental evaluation of nitrate reduction to ammonia on rhodium, J. Catal. 402 (2021) 1–9.

[17] K. Kim, A. Zagalskaya, J.L. Ng, J. Hong, V. Alexandrov, T.A. Pham, X. Su, Coupling nitrate capture with ammonia production through bifunctional redox-electrodes, Nat. Commun. 14 (2023) 823.

[18] X. Fu, X. Zhao, X. Hu, K. He, Y. Yu, T. Li, Q. Tu, X. Qian, Q. Yue, M.R. Wasielewski, Y. Kang, Alternative route for electrochemical ammonia synthesis by reduction of nitrate on copper nanosheets, Appl. Mater. Today 19 (2020) 100620.

[19] L. Yue, W. Song, L. Zhang, Y. Luo, Y. Wang, T. Li, B. Ying, S. Sun, D. Zheng, Q. Liu, A. Farouk, M.S. Hamdy, S. Alfaifi, X. Sun, Recent advance in heterogenous electrocatalysts for highly selective nitrite reduction to ammonia under ambient condition, Small Struct. 3 (2023) 2300168.

[20] Y. Arikawa, Y. Otsubo, H. Fujino, S. Horiuchi, E. Sakuda, K. Umakoshi, Nitrite reduction cycle on a dinuclear ruthenium complex producing ammonia, J. Am. Chem. Soc. 140 (2018) 842–847.

[21] Q. Liu, G. Wen, D. Zhao, L. Xie, S. Sun, L. Zhang, Y. Luo, A. Ali Alshehri, M. S. Hamdy, Q. Kong, X. Sun, Nitrite reduction over Ag nanoarray electrocatalyst for ammonia synthesis, J. Colloid Interface Sci. 623 (2022) 513–519.

[22] M. Xie, S. Tang, Z. Li, M. Wang, Z. Jin, P. Li, X. Zhan, H. Zhou, G. Yu, Intermetallic single-atom alloy In–Pd bimetallene for neutral electrosynthesis of ammonia from nitrate, J. Am. Chem. Soc. 145 (2023) 13957–13967.

[23] H. Jiang, G.-F. Chen, O. Savateev, J. Xue, L.-X. Ding, Z. Liang, M. Antonietti, H. Wang, Enabled efficient ammonia synthesis and energy supply in a zinc–nitrate battery system by separating nitrate reduction process into two stages, Angew. Chem. Int. Ed. 62 (2023) e202218717.

[24] H. Du, H. Guo, K. Wang, X. Du, B.A. Beshiwork, S. Sun, Y. Luo, Q. Liu, T. Li, X. Sun, Durable electrocatalytic reduction of nitrate to ammonia over defective pseudobrookite Fe_2TiO_5 nanofibers with abundant oxygen vacancies, Angew. Chem. Int. Ed. 62 (2023) e202215782.

[25] R. Zhang, S. Zhang, Y. Guo, C. Li, J. Liu, Z. Huang, Y. Zhao, Y. Li, C. Zhi, A. Zn–nitrite, battery as an energy-output electrocatalytic system for high-efficiency ammonia synthesis using carbon-doped cobalt oxide nanotubes, Energy Environ. Sci. 15 (2022) 3024–3032.

[26] M.J. Liu, D.M. Miller, W.A. Tarpeh, Reactive separation of ammonia from wastewater nitrate via molecular electrocatalysis, Environ. Sci. Technol. Lett. 10 (2023) 458–463.

[27] T. Hu, C. Wang, M. Wang, C.M. Li, C. Guo, Theoretical insights into superior nitrate reduction to ammonia performance of copper catalysts, ACS Catal. 11 (2021) 14417–14427.

[28] T. Zhu, Q. Chen, P. Liao, W. Duan, S. Liang, Z. Yan, C. Feng, Single-atom Cu catalysts for enhanced electrocatalytic nitrate reduction with significant alleviation of nitrite production, Small 16 (2020) 2004526.

[29] Y. Zhao, Y. Liu, Z. Zhang, Z. Mo, C. Wang, S. Gao, Flower-like open-structured polycrystalline copper with synergistic multi-crystal plane for efficient electrocatalytic reduction of nitrate to ammonia, Nano Energy 97 (2022) 107124.

[30] L. Wu, J. Feng, L. Zhang, S. Jia, X. Song, Q. Zhu, X. Kang, X. Xing, X. Sun, B. Han, Boosting electrocatalytic nitrate-to-ammonia via tuning of N-intermediate adsorption on a Zn–Cu catalyst, Angew. Chem. Int. Ed. 62 (2023) e202307952.

[31] J. Li, H. Liu, F. Du, L. Liu, Y. Gu, C. Li, C. Guo, H. Wang, Microenvironmental corrosion and hydrolysis induced two-dimensional heterojunction of copper oxide@ferriferous oxide for efficient electrochemical nitrate reduction to ammonia, Chem. Eng. J. 471 (2023) 144488.

[32] J.-Y. Fang, Q.-Z. Zheng, Y.-Y. Lou, K.-M. Zhao, S.-N. Hu, G. Li, O. Akdim, X.-Y. Huang, S.-G. Sun, Ampere-level current density ammonia electrochemical synthesis using CuCo nanosheets simulating nitrite reductase bifunctional nature, Nat. Commun. 13 (2022) 7899.

[33] Y. Wang, A. Xu, Z. Wang, L. Huang, J. Li, F. Li, J. Wicks, M. Luo, D.-H. Nam, C.-S. Tan, Y. Ding, J. Wu, Y. Lum, C.-T. Dinh, D. Sinton, G. Zheng, E.H. Sargent, Enhanced nitrate-to-ammonia activity on copper–nickel alloys via tuning of intermediate adsorption, J. Am. Chem. Soc. 142 (2020) 5702–5708.

[34] G.A. Cerrón-Calle, A.S. Fajardo, C.M. Sánchez-Sánchez, S. Garcia-Segura, Highly reactive Cu-Pt bimetallic 3D-electrocatalyst for selective nitrate reduction to ammonia, Appl. Catal. B Environ. 302 (2022) 120844.

[35] H. Yin, Z. Chen, S. Xiong, J. Chen, C. Wang, R. Wang, Y. Kuwahara, J. Luo, H. Yamashita, Y. Peng, J. Li, Alloying effect-induced electron polarization drives nitrate electroreduction to ammonia, Chem. Catal. 1 (2021) 1088–1103.

[36] W. Gao, K. Xie, J. Xie, X. Wang, H. Zhang, S. Chen, H. Wang, Z. Li, C. Li, Alloying of Cu with Ru enabling the relay catalysis for reduction of nitrate to ammonia, Adv. Mater. 35 (2023) 2202952.

[37] Y. Zhang, X. Chen, W. Wang, L. Yin, J.C. Crittenden, Electrocatalytic nitrate reduction to ammonia on defective Au_1Cu (111) single-atom alloys, Appl. Catal. B Environ. 310 (2022) 121346.

[38] Y. Liu, J. Ma, S. Huang, S. Niu, S. Gao, Highly dispersed copper-iron nanoalloy enhanced electrocatalytic reduction coupled with plasma oxidation for ammonia synthesis from ubiquitous air and water, Nano Energy 117 (2023) 108840.

[39] J. Cai, Y. Wei, A. Cao, J. Huang, Z. Jiang, S. Lu, S.-Q. Zang, Electrocatalytic nitrate-to-ammonia conversion with ~100% Faradaic efficiency via single-atom alloying, Appl. Catal. B Environ. 316 (2022) 121683.

[40] J. Li, J. Gao, T. Feng, H. Zhang, D. Liu, C. Zhang, S. Huang, C. Wang, F. Du, C. Li, C. Guo, Effect of supporting matrixes on performance of copper catalysts in electrochemical nitrate reduction to ammonia, J. Power Sources 511 (2021) 230463.

[41] M. Dadashi Firouzjaei, M. Karimiziarani, H. Moradkhani, M. Elliott, B. Anasori, MXenes: the two-dimensional influencers, Mater. Today Adv. 13 (2022) 100202.

[42] Z. Sofer, X. Wang, M. Yu, MXene chemistry and applications, Small Methods 7 (2023) 2300778.

[43] H. Meng, Y. Yang, T. Shen, W. Liu, L. Wang, P. Yin, Z. Ren, Y. Niu, B. Zhang, L. Zheng, H. Yan, J. Zhang, F.-S. Xiao, M. Wei, X. Duan, A strong bimetal-support interaction in ethanol steam reforming, Nat. Commun. 14 (2023) 3189.

[44] R. Belgamwar, R. Verma, T. Das, S. Chakraborty, P. Sarawade, V. Polshettiwar, Defects tune the strong metal–support interactions in copper supported on defected titanium dioxide catalysts for CO_2 reduction, J. Am. Chem. Soc. 145 (2023) 8634–8646.

[45] Y. Li, H. Shao, Z. Lin, J. Lu, L. Liu, B. Duployer, P.O.Å. Persson, P. Eklund, L. Hultman, M. Li, K. Chen, X.-H. Zha, S. Du, P. Rozier, Z. Chai, E. Raymundo-Piñero, P.-L. Taberna, P. Simon, Q. Huang, A general Lewis acidic etching route for preparing MXenes with enhanced electrochemical performance in non-aqueous electrolyte, Nat. Mater. 19 (2020) 894–899.

[46] B. Fu, J. Sun, C. Wang, C. Shang, L. Xu, J. Li, H. Zhang, MXenes: MXenes: synthesis, optical properties, and applications in ultrafast photonics, Small 17 (2021) 2170048.

[47] P. Huang, H. Ying, S. Zhang, Z. Zhang, W.-Q. Han, Molten salts etching route driven universal construction of MXene/transition metal sulfides heterostructures with interfacial electronic coupling for superior sodium storage, Adv. Energy Mater. 12 (2022) 2202052.

[48] S. Zhao, J. Wang, P. Wang, S. Wang, J. Li, One-step synthesis of N, P co-doped porous carbon electrocatalyst for highly efficient nitrogen fixation, Nano Res. 15 (2022) 1779–1785.

[49] Y. Bai, C. Liu, T. Chen, W. Li, S. Zheng, Y. Pi, Y. Luo, H. Pang, MXene-copper/cobalt hybrids via Lewis acidic molten salts etching for high performance symmetric supercapacitors, Angew. Chem. Int. Ed. 60 (2021) 25318–25322.

[50] M. Xie, F. Dai, H. Guo, P. Du, X. Xu, J. Liu, Z. Zhang, X. Lu, Improving electrocatalytic nitrogen reduction selectivity and yield by suppressing hydrogen evolution reaction via electronic metal–support interaction, Adv. Energy Mater. 13 (2023) 2203032.

[51] Y. Shi, Z.-R. Ma, Y.-Y. Xiao, Y.-C. Yin, W.-M. Huang, Z.-C. Huang, Y.-Z. Zheng, F.-Y. Mu, R. Huang, G.-Y. Shi, Y.-Y. Sun, X.-H. Xia, W. Chen, Electronic metal–support interaction modulates single-atom platinum catalysis for hydrogen evolution reaction, Nat. Commun. 12 (2021) 3021.

[52] W. Yu, J. Yu, M. Huang, Y. Wang, Y. Wang, J. Li, H. Liu, W. Zhou, Laser-controlled tandem catalytic sites of CuNi alloys with ampere-level electrocatalytic nitrate-to-ammonia reduction activities for Zn–nitrate batteries, Energy Environ. Sci. 16 (2023) 2991–3001.

[53] Y. Bu, C. Wang, W. Zhang, X. Yang, J. Ding, G. Gao, Electrical pulse-driven periodic self-repair of Cu-Ni tandem catalyst for efficient ammonia synthesis from nitrate, Angew. Chem. Int. Ed. 62 (2023) e202217337.

[54] G.-Y. Xu, M.-F. Yue, Z.-X. Qian, Z.-Y. Du, X.-Q. Xie, W.-P. Chen, Y.-J. Zhang, J.-F. Li, Metal-support interactions alter the active species on IrO_x for electrocatalytic water oxidation, J. Mater. Chem. A 11 (2023) 15204–15210.

[55] S. Han, H. Li, T. Li, F. Chen, R. Yang, Y. Yu, B. Zhang, Ultralow overpotential nitrate reduction to ammonia via a three-step relay mechanism, Nat. Catal. 6 (2023) 402–414.

[56] P. Li, Z. Jin, Z. Fang, G. Yu, A single-site iron catalyst with preoccupied active centers that achieves selective ammonia electrosynthesis from nitrate, Energy Environ. Sci. 14 (2021) 3522–3531.

[57] Z. Zhang, Y. Liu, X. Su, Z. Zhao, Z. Mo, C. Wang, Y. Zhao, Y. Chen, S. Gao, Electro-triggered Joule heating method to synthesize single-phase CuNi nano-alloy catalyst for efficient electrocatalytic nitrate reduction toward ammonia, Nano Res. 16 (2023) 6632–6641.

[58] S. Liu, L. Cui, S. Yin, H. Ren, Z. Wang, Y. Xu, X. Li, L. Wang, H. Wang, Heterointerface-triggered electronic structure reformation: Pd/CuO nano-olives motivate nitrite electroreduction to ammonia, Appl. Catal. B Environ. 319 (2022) 121876.

[59] L. Ouyang, X. He, S. Sun, Y. Luo, D. Zheng, J. Chen, Y. Li, Y. Lin, Q. Liu, A.M. Asiri, X. Sun, Enhanced electrocatalytic nitrite reduction to ammonia over P-doped TiO_2 nanobelt array, J. Mater. Chem. A 10 (2022) 23494–23498.

[60] H. Wang, F. Zhang, M. Jin, D. Zhao, X. Fan, Z. Li, Y. Luo, D. Zheng, T. Li, Y. Wang, B. Ying, S. Sun, Q. Liu, X. Liu, X. Sun, V-doped TiO_2 nanobelt array for high-efficiency electrocatalytic nitrite reduction to ammonia, Mater. Today Phys. 30 (2023) 100944.

[61] Y. Zhang, Y. Wan, X. Liu, K. Chen, K. Chu, Nb-doped NiO nanoflowers for nitrite electroreduction to ammonia, iScience 26 (2023) 107944.

[62] J. Xiang, H. Zhao, K. Chen, X. Li, X. Li, K. Chu, Atomically dispersed Pd on defective BN nanosheets for nitrite electroreduction to ammonia, J. Colloid Interface Sci. 653 (2024) 390–395.

[63] C. Xu, Y. Liang, X. He, A. Zhang, L. Ouyang, L. Hu, X. Fan, Y. Luo, D. Zheng, S. Sun, A. Farouk, M.S. Hamdy, X. Sun, $ZnFe_2O_4$ nanosheet array: a highly efficient electrocatalyst for ambient ammonia production via nitrite reduction, Catal. Sci. Technol. 14 (2024) 57–61.

[64] L. Hu, D. Zhao, C. Liu, Y. Liang, D. Zheng, S. Sun, Q. Li, Q. Liu, Y. Luo, Y. Liao, L. Xie, X. Sun, Amorphous CoB nanoarray as a high-efficiency electrocatalyst for nitrite reduction to ammonia, Inorg. Chem. Front. 9 (2022) 6075–6079.

[65] Y. Guo, R. Zhang, S. Zhang, Y. Zhao, Q. Yang, Z. Huang, B. Dong, C. Zhi, Pd doping-weakened intermediate adsorption to promote electrocatalytic nitrate reduction on TiO_2 nanoarrays for ammonia production and energy supply with zinc–nitrate batteries, Energy Environ. Sci. 14 (2021) 3938–3944.

[66] Z. Zhang, W. Shi, W. Wang, Y. Xu, X. Bao, R. Zhang, B. Zhang, Y. Guo, F. Cui, Interfacial electronic effects of palladium nanocatalysts on the by-product ammonia selectivity during nitrite catalytic reduction, Environ. Sci. Nano 5 (2018) 338–349.

[67] Y. Zhang, Y. Wang, L. Han, S. Wang, T. Cui, Y. Yan, M. Xu, H. Duan, Y. Kuang, X. Sun, Nitrite electroreduction to ammonia promoted by molecular carbon dioxide with near-unity Faradaic efficiency, Angew. Chem. Int. Ed. 62 (2023) e202213711.

[68] F.-Y. Chen, Z.-Y. Wu, S. Gupta, D.J. Rivera, S.V. Lambeets, S. Pecaut, J.Y.T. Kim, P. Zhu, Y.Z. Finfrock, D.M. Meira, G. King, G. Gao, W. Xu, D.A. Cullen, H. Zhou, Y. Han, D.E. Perea, C.L. Muhich, H. Wang, Efficient conversion of low-concentration nitrate sources into ammonia on a Ru-dispersed Cu nanowire electrocatalyst, Nat. Nanotechnol. 17 (2022) 759–767.

[69] K. Fan, W. Xie, J. Li, Y. Sun, P. Xu, Y. Tang, Z. Li, M. Shao, Active hydrogen boosts electrochemical nitrate reduction to ammonia, Nat. Commun. 13 (2022) 7958.

[70] J. Xu, S. Zhang, H. Liu, S. Liu, Y. Yuan, Y. Meng, M. Wang, C. Shen, Q. Peng, J. Chen, X. Wang, L. Song, K. Li, W. Chen, Breaking local charge symmetry of iron

single atoms for efficient electrocatalytic nitrate reduction to ammonia, Angew. Chem. Int. Ed., e202308044.

[71] Z. Luo, X. Li, T. Zhou, Y. Guan, J. Luo, L. Zhang, X. Sun, C. He, Q. Zhang, Y. Li, X. Ren, Engineering energy level of FeN_4 sites via dual-atom site construction toward efficient oxygen reduction, Small 19 (2023) 2205283.

[72] Q. Wang, J. Su, H. Chen, D. Wang, X. Tian, Y. Zhang, X. Feng, S. Wang, J. Li, H. Jin, Highly conductive nitrogen-doped sp^2/sp^3 hybrid carbon as a conductor-free charge storage host, Adv. Funct. Mater. 32 (2022) 2209201.